Article

Low-Frequency Dynamic Magnetic Fields Decrease Cellular Uptake of Magnetic Nanoparticles

Anna V. Ivanova [1,†], Nelly S. Chmelyuk [1,†], Aleksey A. Nikitin [1,2], Alexander G. Majouga [3], Vladimir P. Chekhonin [1,4] and Maxim A. Abakumov [1,*]

1   Department of Medical Nanobiotechnology, N.I. Pirogov Russian National Research Medical University, 117997 Moscow, Russia; super.fosforit@yandex.ru (A.V.I.); nellichmelyuk@yandex.ru (N.S.C.); nikitin.aa93@mail.ru (A.A.N.); chekhoninnew@yandex.ru (V.P.C.)

2   Department of General and Inorganic Chemistry, Mendeleev University of Chemical Technology of Russia, 125047 Moscow, Russia

3   Laboratory of Biomedical Nanomaterials, National University of Science and Technology (MISIS), 119049 Moscow, Russia; alexander.majouga@gmail.com

4   Department of Basic and Applied Neurobiology, Serbsky National Medical Research Center for Psychiatry and Narcology, 119991 Moscow, Russia

*   Correspondence: abakumov1988@gmail.com; Tel.: +7-9035864777

†   These authors contributed equally to this work.

Abstract: Magnetic nanoparticles have gained attention as a potential structure for therapy and diagnosing oncological diseases. The key property of the magnetic nanoparticles is the ability to respond to an external magnetic field. It is known that magnetofection causes an increase in the cellular uptake of RNA and DNA in complexes with magnetic nanoparticles in the presence of a permanent magnetic field. However, the influence of a dynamic magnetic field on the internalization of MNPs is not clear. In this work, we propose the idea that applying external low-frequency dynamic magnetic fields may decrease the cellular uptake, such as macrophages and malignant neuroblastoma. Using fluorescence microscopy and atomic emission spectroscopy, we found that oscillating magnetic fields decreased the cellular uptake of magnetic nanoparticles compared to untreated cells by up to 46%. In SH-SY5Y tumor cells and macrophage RAW264.7 cells, the absolute values of Fe per cell differed by 0.10 pg/cell and 0.33 pg/cell between treated and untreated cells, respectively. These results can be applied in the control of the cellular uptake in different areas of biomedicine.

Keywords: magnetic nanoparticles; low-frequency dynamic magnetic field; macrophages; cell uptake; MNP uptake

1. Introduction

Nowadays, magnetic nanoparticles (MNPs) have gained attention as a biocompatible material for pathology imaging using MRI [1–6], cancer treatment by magnetic hyperthermia [7–11], drug delivery [12–15], the separation of cells [16–19], DNA [20], and other molecules for more than several decades. In most cases, the MNPs' composition includes a significant amount of magnetite or transition metal ferrites making them nanomaterials that can be controlled by an external magnetic field [21].

If the gradient magnetic field is applied to the MNPs, the migration of the MNPs to the magnet will be observed. Magnetofection is a well-known technique that utilizes the ability of the MNPs to increase their internalization by simply applying a static magnetic field created by a permanent magnet or direct current electromagnetic field [22]. Compared to the standard transfection protocol in vitro [23], this approach improved the transfection efficiency, provided non-viral gene delivery, used an adenoviral formulation in vivo in rats' ilea lumens and mice's stomach lumens, where pH values are exceptionally high and degradative enzymes are present, provided knockout proteins through oligonucleotide

delivery [24], and gene therapy for various diseases, including melanoma tumors using siRNA [25]. In these cases, the MNPs were accumulated near the cell membranes using static magnetic fields, thus increasing the effectiveness of the intracellular transport pathways. Additionally, Jiang et al. developed the magnet-mediated delivery approach, which applies the static magnetic field to the tumor region, leading to an increase in the uptake of MNPs by the tumor in vivo [26].

In case of exposure to a dynamic magnetic field (DMF), the result depends on the type of relaxation of MNPs. It is known that when they are exposed to an external dynamic magnetic field, the type of relaxation (Néel or Brownian) is determined by a combination of parameters, such as the field frequency, the size of the magnetic core, and the superparamagnetic/ferromagnetic state of the MNPs [27]. Néel or Brownian relaxations coexist in a wide frequency range from several kHz to hundreds of kHz [28–30]. However, at DMF frequencies < 10 kHz, other parameters being equal, the Brownian relaxation of the MNPs dominates over the Néel relaxation [27,29]. Different relaxation mechanisms of the MNPs in a DMF can lead to the conversion of the field energy into either heat (hyperthermia) or into mechanical movements (magnetomechanics) [31]. Deissler et al. showed that for 20 nm magnetite nanoparticles magnetized in a DMF with various frequencies, the magnetization of such nanoparticles due to the Néel relaxation mechanism lags behind that of the Brownian, even at $f = 10$ kHz and $B = 100$ mT [32], leading to the mechanical rotation of the MNPs, but not heating. As was shown by magnetic force microscopy, the individual nanoparticles possess enhanced magnetic properties in comparison with aggregates or powder, thus making individual magnetic nanoparticles a more prospective material to be used in magnetomechanics [33,34].

Nanoparticles, particularly MNPs, can be internalized by cells through various mechanisms of endocytosis: phagocytosis (only for phagocytes), clathrin-mediated endocytosis [35,36], caveolin-mediated endocytosis, clathrin-/caveolae-independent endocytosis, and micropinocytosis [37]. For each mechanism, the MNPs must be in contact with the cell membrane, interacting with the extracellular environment for some period. The effects of low-frequency dynamic magnetic fields (LF DMF) on cells are complex and depend on various factors, such as the type of cells, field frequency, intensity and duration of exposure, and the presence of various additives. Extremely LF DMF (<1 kHz) on the order of mT are known to contribute to the increased cellular uptake of non-magnetic drugs such as methotrexate [38] and doxorubicin [39]. It was proposed that membrane-charged lipids could align along the magnetic field vector, resulting in the formation of transient membrane pores or damage large enough to allow medium-sized molecules to pass through them. Moreover, the combination of doxorubicin with LF DMF resulted in an increased amount of intracellular reactive oxygen species and decreased the cell survival rate of tumor cells [39]. On the other hand, when an LF DMF is applied, the MNPs undergo rotational–oscillatory movements to align their magnetic moment to the applied field direction in accordance with the Brownian relaxation mechanism. We propose that MNPs' magneto-mechanical movements in an LF DMF may influence these interactions, in particular, decreasing the time spent by the MNPs near the membrane, reducing the probability of vesicle formation and internalization inside the cell. Contrary to magnet-mediated MNP delivery, this approach leads to an overall decrease in the cellular uptake. These effects can be used for the control of the kinetic uptake of the MNPs by cells in in vitro experiments, reducing cellular internalization when it is necessary.

In this work, we studied the LF DMF's influence on the time-dependent internalization of iron oxide MNPs with two different types of frequently used functional coatings (polyethylene glycol and human serum albumin) for two different cell lines responsible for an unspecific uptake, such as malignant neuroblastoma SH-SY5Y and macrophages RAW264.7. Albumin-based nanoparticles offer several advantages, such as biocompatibility, biodegradability, and, most importantly, the passive targeting of tumor cells due to receptor-mediated transcytosis, such as SPARC, gp30, gp18, etc. [40]. These cell types have

very different abilities for cellular uptake, so macrophages are known to be phagocytic cells, and SH-SY5Y cells have specific receptors for albumin.

2. Materials and Methods

2.1. Materials

Oleic acid (OA), iron (III) chloride ($FeCl_3$), 1-octadecene (1-ODE), hexane, 2-propanol, ethanol, sodium hydroxide (NaOH), 3,4-dihydroxyphenylacetic acid (DOPAC), N-hydroxyc uccinimide (NHS), 1-Ethyl-3-(3-dymethylaminopropyl) carbodiimide (EDC), phosphate-buffered saline (PBS), dimethyl sulfoxide (DMSO), and human serum albumin (HSA) were purchased from (Sigma–Aldrich, Burlington, MA, USA). Poly(ethylene glycol) 2-aminoethyl ether acetic acid (NH2-PEG-COOH, Mn ~ 2000 g/mol) was purchased from (BLD Phar-matech, Shanghai, China). Sodium oleate (NaOL) was purchased from (Abcr® GmbH Karlsruhe, Baden-Württemberg, Karlsruhe, Germany). Cyanine5-amine (Cy5-amine) was purchased from (Luminprobe Biotech Industry Ltd., Moscow, Russia). Methanol was purchased from (AO Reachem, Moscow, Russia). Paraformaldehyde was purchased from (Panreac, Castellar del Vallés, Catalonia, Spain). Dulbecco's Modified Eagle Medium: Nutrient Mixture F12 (DMEM/F12) and TrypLE were purchased from (Wuhan Servicebio Technology, Wuhan, China). Roswell Park Memorial Institute medium (RPMI), fetal bovine serum (FBS), Dulbecco's modified phosphate saline buffer (DPBS), L-glutamine solution, and penicillin/streptomycin solution were purchased from (Gibco, Waltham, MA, USA).

2.2. Methods

2.2.1. Synthesis of Fe_3O_4

The synthesis of the oleate complex and magnetic nanoparticles Fe_3O_4 was carried out according to the method described previously [41].

2.2.2. Characterization of MNP

Microphotographs of Fe_3O_4 samples were obtained by transmission electron microscopy using a JEOL JEM-1400 120 kV microscope (JEOL, Akishima, Tokyo, Japan). A drop of a freshly prepared Fe_3O_4 sample was applied to a perforated copper mesh (300 cells) coated with Formvar®. The sample was then left to dry completely. The size distribution of the Fe_3O_4 was assessed using ImageJ software (version 1.8.0_172). For each sample, at least 1000 MNPs were analyzed. The size-distribution analysis was performed using a Gaussian distribution function using Origin 2018 software.

Measurements of the static magnetic properties (from −1500 to 1500 kA/m, 300 K) were carried out on a Quantum Design PPPMS-9 device (Quantum Design, San Diego, CA, USA) with an oscillation amplitude of 2 mm and a frequency of 40 Hz.

The hydrodynamic size of the Fe_3O_4 was determined by dynamic light scattering using a Malvern Zetasizer Nano ZS device (Malvern Pananalytical, Malvern, Worcestershire, UK) at 25 °C. A solution of Fe_3O_4 with a concentration of 0.2 μg/mL was prepared in the solvent in which the reaction was carried out.

2.2.3. Surface Modification Fe_3O_4 with 3,4-dihydroxyphenylacetic Acid (Fe_3O_4-DOPAC)

24 mg of sodium hydroxide (NaOH) was dissolved in 10 mL of anhydrous methanol (CH_3OH), followed by the addition of 51 mg of 3,4-dihydroxyphenylacetic acid (DOPAC) and 10 mL of Fe_3O_4 in hexane with a concentration of [Fe] = 0.5 mg/mL. The resulting mixture was incubated for 5 h in a water bath at 50 °C with continuous stirring on a magnetic stirrer (530 rpm).

At the end of the reaction, the Fe_3O_4-DOPAC was separated from the solution by centrifugation (6000 rpm, 20 min), the supernatant liquid was poured off, and the precipitate (Fe_3O_4-DOPAC) was dried in a stream of argon to remove the remaining hexane and methanol. Then, the functionalized MNPs were resuspended in 10 mL of deionized water, the solution was washed on Millipore® Amicon Ultra-4, MWCO 30 kDa centrifuge filters, concentrated to 1 mL, and, additionally, sequentially passed through Millipore syringe

filters with pore sizes of 0.45 μm and 0.22 μm, respectively, to remove any possible Fe_3O_4-DOPAC aggregates. The overall yield after the modification of the MNPs with DOPAC was equal to 70%.

2.2.4. Surface Modification Fe_3O_4-DOPAC with Human Serum Albumin (Fe_3O_4-DOPAC-HSA)

We mixed 2 mL of Fe_3O_4-DOPAC in water with a concentration of [Fe] = 0.25 mg/mL, 8 μL of NHS in water with a concentration (10 mg/mL), 14 μL of EDC in water with a concentration (10 mg/mL), and stirred at room temperature for 15 min. The excess of NHS and EDC were purified using a PD-10 mini-column. After the incubation time, 10μL with a concentration (10 mg/mL) of HSA was added and stirred at room temperature for 12 h. The Fe_3O_4-DOPAC-HSA was washed to remove free HSA on the centrifuge filters (Millipore Amicon Ultra-4, MWCO 100 kDa) 8 times with PBS and, additionally, sequentially passed through Millipore syringe filters with pore sizes of 0.45 μm and 0.22 μm, respectively, to remove any possible Fe_3O_4-DOPAC-HSA aggregates.

2.2.5. Functionalization of the Surface of Fe_3O_4-DOPAC and Fe_3O_4-DOPAC-HSA with an Aminocarboxy Derivative of PEG (Fe_3O_4-DOPAC-PEG and Fe_3O_4-DOPAC-HSA-PEG)

We mixed 1 mL of Fe_3O_4-DOPAC in water and Fe_3O_4-DOPAC-HSA in PBS with a concentration of [Fe] = 1 mg/mL, 8 μL of NHS in water with a concentration (10 mg/mL), 14 μL of EDC in water with a concentration (10 mg/mL), and stirred at room temperature for 15 min. The excess NHS and EDC were purified using a PD-10 mini-column. After the incubation time, 100 μL with a concentration (100 mg/mL) of poly(ethylene glycol) 2-aminoethyl ether of acetic acid (PEG, Mn ~ 2000 g/mol) in water were added and stirred at room temperature for 12 h. The excess of PEG was purified using a PD-10 mini-column and, additionally, sequentially passed through Millipore syringe filters with pore sizes of 0.45 μm and 0.22 μm, respectively, to remove any possible Fe_3O_4-DOPAC-PEG and Fe_3O_4-DOPAC-HSA-PEG aggregates.

2.2.6. Functionalization of the Surface of Fe_3O_4-DOPAC-PEG and Fe_3O_4-DOPAC-HSA-PEG with Cy5 Fluorescent Label (Fe_3O_4-DOPAC-PEG-Cy5 and Fe_3O_4-DOPAC-HSA-PEG)

We added 16 μL of NHS in PBS with a concentration (10 mg/mL) and 32 μL of EDC in PBS with a concentration (10 mg/mL) to 1 mL of Fe_3O_4-DOPAC-PEG and Fe_3O_4-DOPAC-HSA-PEG ([Fe] = 1 mg/mL) and incubated at room temperature for 15 min. Next, we added 10 μL of Cy5-amine in DMSO with a concentration (10 mg/mL). The mixture was then incubated with fluorescent labels at room temperature for 12 h. The excess of Cy5-amine was purified using a PD-10 mini-column filled with Sephadex G-25 and eluted with PBS.

2.2.7. Internalization Experiments and Confocal Imaging

We cultured the SH-SY5Y cells in DMEM/F12 media containing antibiotics (100 U/mL penicillin, 100 mg/mL streptomycin), L-glutamine (2 mM), and 10% FBS. RAW264.7 cells were cultured in RPMI 1640 media containing antibiotics (100 U/mL penicillin, 100 mg/mL streptomycin), L-glutamine (2 mM), and 10% FBS. The cells were cultured in T-75 cultural flasks (Corning, New York, NY, USA) under standard conditions (37 °C and 5% CO_2). When the cells reached a high confluence, we subcultured them at a ratio of 1:4–1:6 using the standard trypsinization method.

2.2.8. Measurement of Intracellular Iron Content with Atomic Emission Spectroscopy (AES)

The SH-SY5Y and RAW264.7 cells were placed in 6-well plates (5×10^5 cells/well) and incubated for 24 h without treatment at 37 °C and 5% CO_2. To investigate the iron accumulation in the cells, the growth medium was replaced and supplemented with Fe_3O_4 (Fe_3O_4-DOPAC-PEG-Cy5 or Fe_3O_4-DOPAC-HSA-PEG-Cy5) with an iron concentration [Fe] of 100 μg/mL. Afterwards, the cells were treated with an oscillatory magnetic field for 60 or 120 min at ambient conditions, excluding control cells. The cells were then thoroughly washed with DPBS, detached with 0.25% trypsin solution, precipitated by centrifugation, and counted. For each measurement, the cell precipitates were dissolved in

200 µL of concentrated nitric acid for 2 h at 60 °C. The iron concentration was measured using an Agilent 4200 MP-AES atomic emission spectrometer (Santa Clara, CA, USA). All experiments were conducted in triplicate. Statistical analysis using "Unpaired *t*-test" was performed using GraphPad Prism 9.0.

2.2.9. Confocal Microscopy

The SH-SY5Y and RAW264.7 cells were seeded in a confocal 35 mm Petri dish (3×10^5 cells/well) and incubated for 24 h without treatment at 37 °C and 5% CO_2. Then, the growth medium was replaced and supplemented with Fe_3O_4 (Fe_3O_4-DOPAC-PEG-Cy5 or Fe_3O_4-DOPAC-HSA-PEG-Cy5) with an iron concentration [Fe] of 100 µg/mL. Afterwards, the cells were treated with an oscillatory magnetic field for 60 or 120 min at ambient conditions, excluding control cells. Then, the cells were washed twice with DPBS and confocal images were obtained using a Nikon Ti2 Eclipse microscope (Ex-Max 642 nm and Em-Max 660 nm) with 25×1.1 water immersion objective lenses (Nikon, Minato, Tokyo, Japan). The average cell intensity was calculated using Fiji software (version 1.6.0-24) (NIH, Bethesda, MD, USA) (calculated for 15–20 areas). Statistical analysis using "Unpaired *t*-test" was performed using GraphPad Prism 9.0.

3. Results

To synthesize MNPs with a narrow size distribution and good crystallinity, a thermal decomposition of iron (III) oleate was performed. As shown in the TEM images, the shape of the obtained MNPs was truncated and the average size of their magnetic core was equal to 14 ± 1 nm (Figure 1 and Supplementary Materials, Figure S1a). The XRD pattern is similar to the Fe_3O_4 XRD pattern from ICDD PDF-2 (No 1513301). The increase in intensity in the 2θ region from 15 to 30° was due to the presence of amorphous organic compounds, e.g., oleic acid (Supplementary Materials, Figure S1b). For the phase transfer from organic media to water functionalization with 3,4-dihydroxyphenylacetic acid (DOPAC), DOPAC-coated MNPs were coated with HSA, followed by an additional functionalization with PEG, or pure PEG molecules. Both DOPAC-PEG and DOPAC-HSA-PEG-coated MNPs were further conjugated with Cyanine 5 (Cy5), resulting in samples named Fe_3O_4-DOPAC-PEG-Cy5 and Fe_3O_4-DOPAC-HSA-PEG-Cy5, respectively. Dynamic light scattering (DLS) measurements of colloid solutions of MNPs was conducted for each step of the functionalization (Supplementary Materials, Figure S1c and Table S1). For the final colloids of Fe_3O_4-DOPAC-PEG-Cy5 and Fe_3O_4-DOPAC-HSA-PEG-Cy5, the hydrodynamic diameters were equal to 38 ± 2 and 39 ± 1 nm by volume and 48 ± 2 and 44 ± 3 nm by intensity, indicating nearly the same size for both samples (Supplementary Table S1).

Measurements of magnetic properties were close to the obtained MNPs' superparamagnetic behavior, with $J_s = 53.5$ A·m^2·kg^{-1} and H_c equal to 1.5 k A·m^{-1} (Supplementary Materials, Figure S1d).

For LF DMF field generation, a permanent N42 neodymium magnet (axial magnetization; $B_r = 1.33$ T; D = 3 cm; L = 1 cm) was fixed to the piston of the stepper motor (Figure 2a). Theoretical calculations showed that the maximal magnetic flux density (40 mT) at the central point of the Petri dish during oscillatory movements of the permanent magnet was reached at point '2' when the permanent magnet was located above the cells. By contrast, at points '1' and '3', the magnetic flux density was minimal and equal to 9 mT, respectively (Figure 2b,c).

Calculating the average fluorescence intensity from the cells helps to semi-quantitatively evaluate the MNPs' uptake efficiency by the cells. As seen in Figure 3a, the integral intensity values increase with the incubation time. In the case of cells exposed to an external LF DMF, lower values of fluorescent intensity were observed compared to cells not treated with LF DMF. A quantitative analysis of the Fe amounts per cell after 1 and 2 h of incubation with MNPs showed an increase in the amount of iron per cell with increased incubation time, and the Fe amount per cell in cells treated with an LF DMF was significantly lower compared to the cells in the control experiment (Figure 3b).
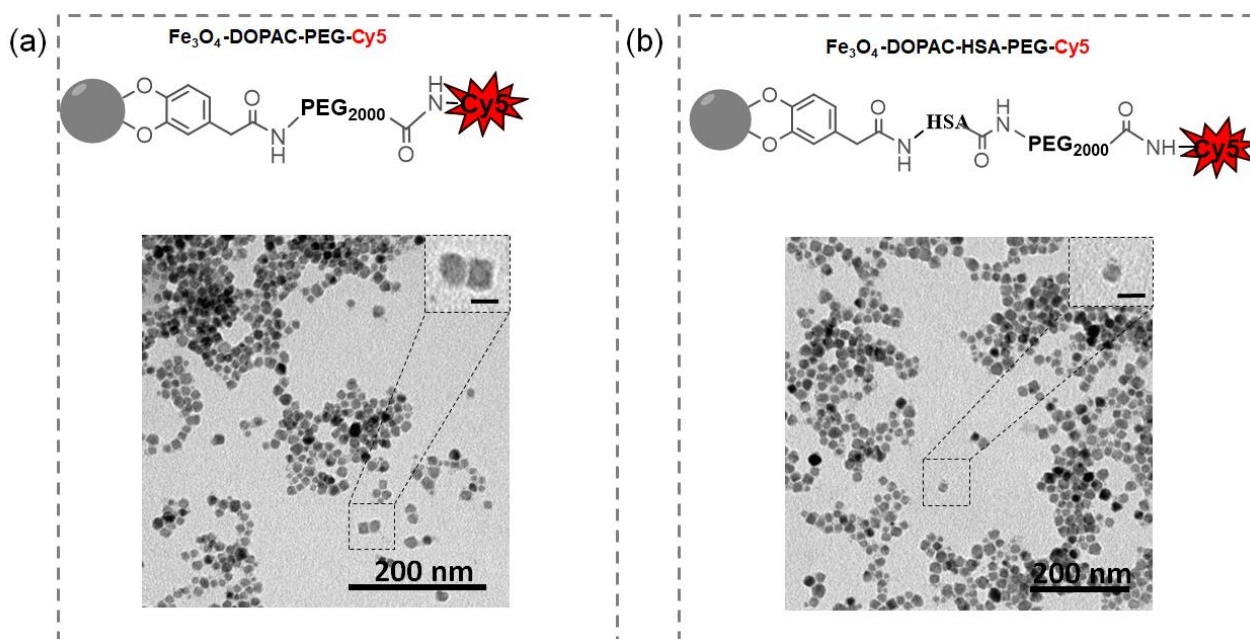
Figure 1. (**a**) Schematic structure and TEM of the Fe$_3$O$_4$-DOPAC-PEG-Cy5. (**b**) Schematic structure and TEM of the Fe$_3$O$_4$-DOPAC-HSA-PEG-Cy5. Scale bar: 200 nm, insert scale bar: 15 nm.
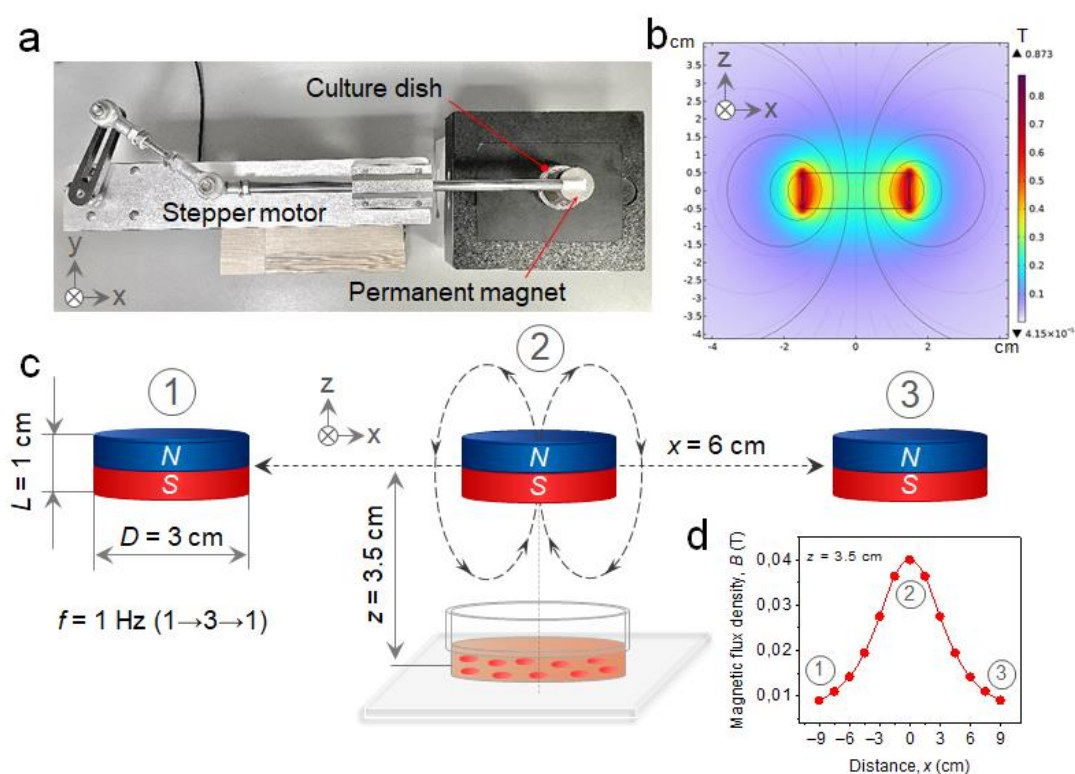
Figure 2. (**a**) Experimental setup consisting of a permanent magnet horizontally oscillating over a culture dish surface. (**b**) 2D model of the magnetic flux density around the permanent magnet reconstructed by COMSOL Multiphysics® software (version 6.1). (**c**) Schematic representation of the experimental setup indicating its main dimensional characteristics. (**d**) Plot of the magnetic flux density at the center point of the culture dish, depending on the displacement of the center of the magnet along the *x*-axis (y = 0, z = 3.5 cm).
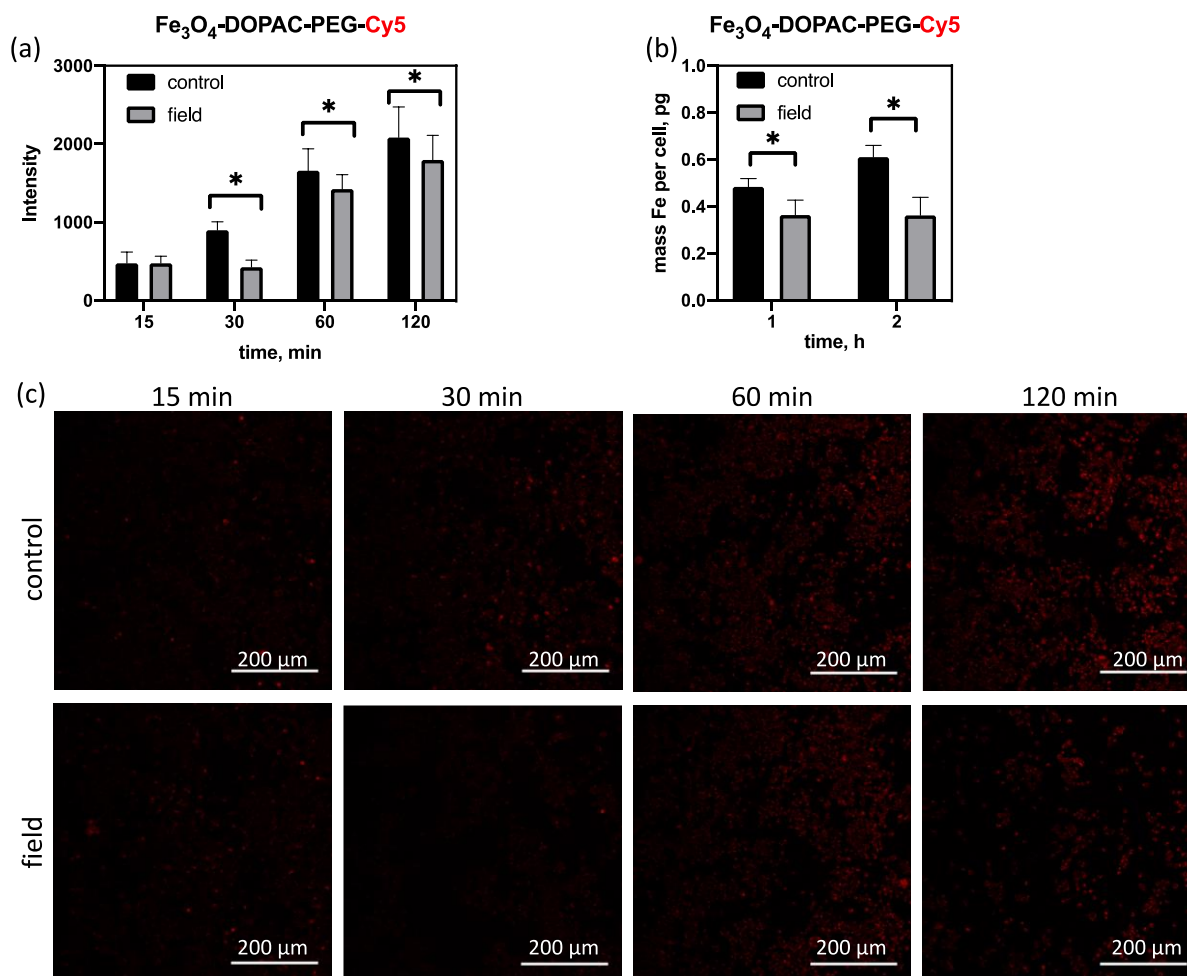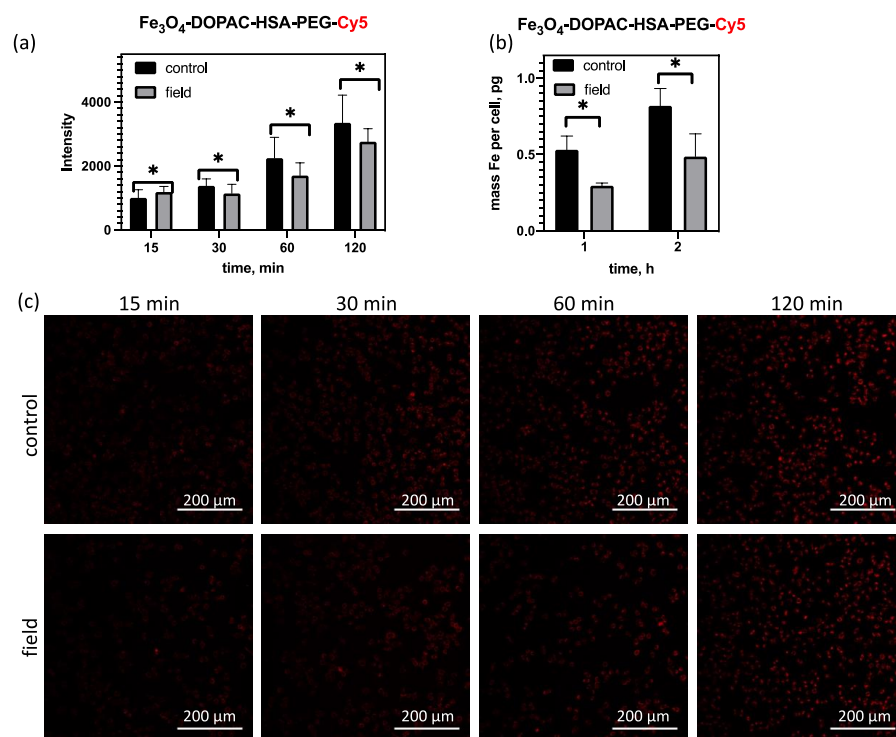
Figure 3. (**a**) Average intensity values of confocal images for RAW264.7 cell areas at various incubation times with Fe$_3$O$_4$-DOPAC-PEG-Cy5, [Fe] = 100 µg/mL, *—*t*-test, significant difference: $p < 0.05$; (**b**) AES measurement of the iron content in RAW264.7 cell areas at various incubation times with Fe$_3$O$_4$-DOPAC-PEG-Cy5, [Fe] = 100 µg/mL, *—*t*-test, significant difference: $p < 0.05$; (**c**) Confocal images of RAW264.7 cells incubated with Fe$_3$O$_4$-DOPAC-PEG-Cy5 in the presence and absence of the external magnetic field, scanning confocal microscopy, scale bar 200 µm.

The incubation of Fe$_3$O$_4$-DOPAC-PEG-Cy5 with RAW264.7 cells showed a time-dependent accumulation of fluorescently labeled MNPs in cells with or without the application of an external magnetic field, indicating that RAW264.7 cells, originally presented in a macrophage cell culture, can internalize MNPs (Figure 3c).

Coating is known to affect the interaction of the nanoparticles with the cells, dramatically changing the intensity of the MNP uptake. We performed similar experiments with MNPs additionally coated with HSA. The Fe$_3$O$_4$-DOPAC-HSA-PEG-Cy5 was internalized faster, and the number of MNPs inside the cells, measured by integral intensity, was almost 1.5 times higher compared to the Fe$_3$O$_4$-DOPAC-PEG-Cy5 (Figure 4a). However, the fluorescence intensity of the MNPs initialized in the cells after an external magnetic field was applied showed the same tendency.

The internalization experiments with fluorescently labeled MNPs on neuroblastoma SH-SY5Y cell lines for Fe$_3$O$_4$-DOPAC-PEG-Cy5 and Fe$_3$O$_4$-DOPAC-HSA-PEG-Cy5 are shown in Figures 5 and 6, respectively.
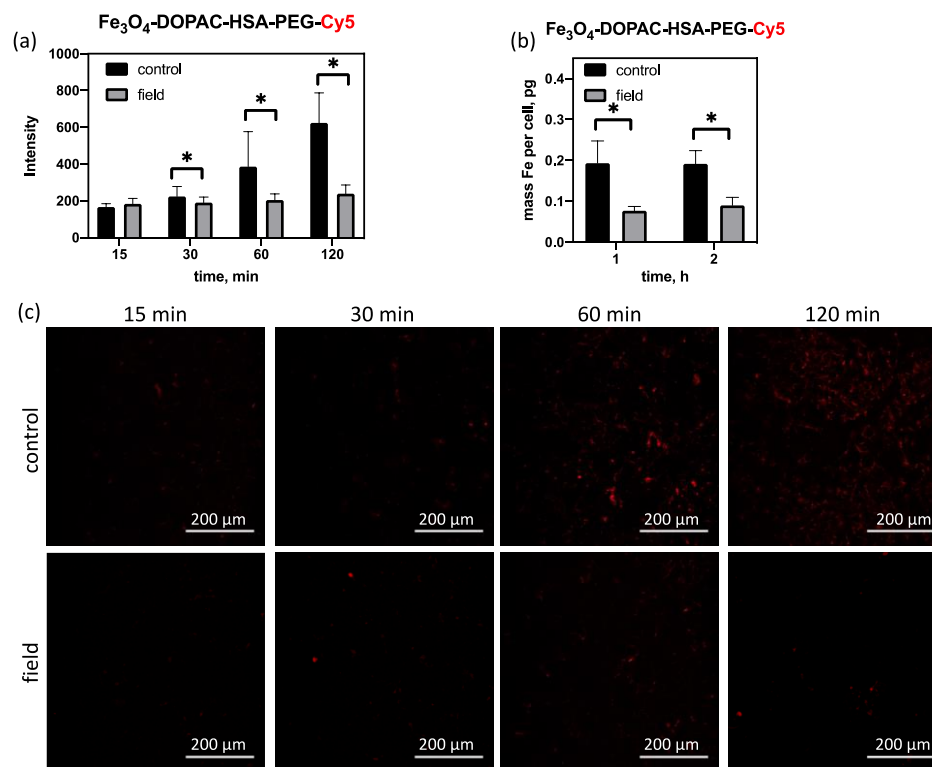
Figure 4. (**a**) Average intensity values of confocal images for RAW264.7 cell areas at various incubation times with Fe_3O_4-DOPAC-HSA-PEG-Cy5, [Fe] = 100 μg/mL, *—*t*-test, significant difference: $p < 0.05$; (**b**) AES measurement of iron content in RAW264.7 cell areas at various incubation times with Fe_3O_4-DOPAC-HSA-PEG-Cy5, [Fe] = 100 μg/mL, *—*t*-test, significant difference: $p < 0.05$; (**c**) Confocal images of RAW264.7 cells, which were incubated with Fe_3O_4-DOPAC-HSA-PEG-Cy5 in the presence and absence of a magnetic field, scanning confocal microscopy, scale bar 200 μm.
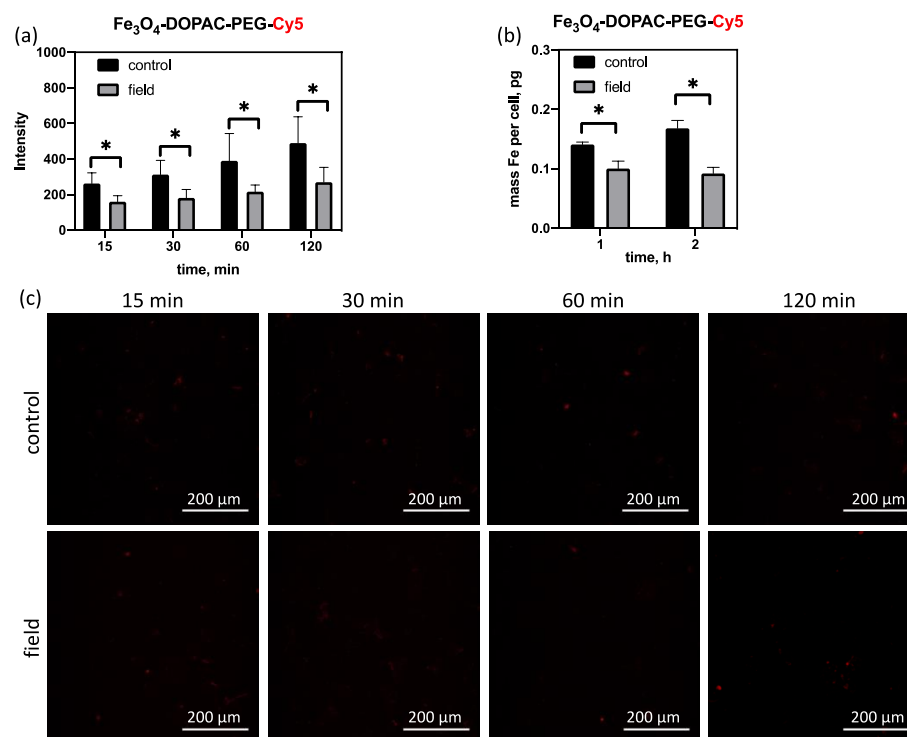
Figure 5. (**a**) Average intensity values of confocal images for SH-SY5Y cell areas at various incubation times with Fe_3O_4-DOPAC-PEG-Cy5, [Fe] = 100 μg/mL, *—*t*-test, significant difference: $p < 0.05$;

(**b**) AES measurement of iron content in SH-SY5Y cell areas at various incubation times with Fe_3O_4-DOPAC-PEG-Cy5, [Fe] = 100 μg/mL, *—*t*-test, significant difference: $p < 0.05$; (**c**) Confocal images of SH-SY5Y cells, which were incubated with Fe_3O_4-DOPAC-PEG-Cy5 in the presence and absence of a magnetic field, scanning confocal microscopy, scale bar 200 μm.

Figure 6. (**a**) Average intensity values of confocal images for SH-SY5Y cell areas at various incubation times with Fe_3O_4-DOPAC-HSA-PEG-Cy5, [Fe] = 100 μg/mL, *—*t*-test, significant difference: $p < 0.05$; (**b**) AES measurement of iron content in SH-SY5Y cell areas at various incubation timed with Fe_3O_4-DOPAC-HSA-PEG-Cy5, [Fe] = 100 μg/mL, *—*t*-test, significant difference: $p < 0.05$; (**c**) Confocal images of SH-SY5Y cells incubated with Fe_3O_4-DOPAC-HSA-PEG-Cy5 in the presence and absence of a magnetic field, scanning confocal microscopy, scale bar 200 μm.

Interestingly, the overall fluorescent intensity in SH-SY5Y cells was significantly lower than in the RAW264.7 cell line; however, the fluorescent intensity increased with an increase in incubation time. For the SH-SY5Y cell line, the effect of applying an LF DMF was more pronounced than in the RAW264.7 cell line (Figures 5 and 6). For the SH-SY5Y cell line, the fluorescence intensity difference between cells with and without an applied external LF DMF was detected up to 2 h and was almost three times lower than without an applied LF DMF. The Fe amount per SH-SY5Y was also significantly lower compared to the RAW264.7 cells, and was equal to about 0.19 and 0.82 pg Fe/cell.

Importantly, the observed effects were the same regardless of how the magnet was moving around the culture plate, namely from the top or from the bottom (Supplementary Figure S2), and these MNPs were non-toxic at the studied concentration (Supplementary Figure S3). The concentration of iron in the cells measured by AES represents a quantitative amount of the MNPs that is associated with the cells; however, some of the MNPs might not be internalized by the cells, but rather be attached to the cell surface or only start to be internalized. The cells were washed with DPBS to remove any MNPs that remained in the culture media or weakly attached to cells. Also, we additionally performed a Prussian Blue staining of the cells, where a clear blue staining of cytoplasm is observed in the case of cells incubated with MNP, whereas blank cells do not show any change in color (Supplementary Figures S4 and S5). The results of the Prussian Blue staining indicates that

the MNPs are indeed internalized into the cells and are in their cytoplasm at least after 2 h of incubation.

4. Discussion

The internalization of nanoparticles, particularly MNPs, with cells during in vitro experiments is an important issue that must be accurately described before translation into in vivo experiments or clinical trials. The size, shape, the chemical structure of the coating, and the surface charge of nanoparticles are known to play an important role in the interaction of nanoparticles with cells [42–46]. By optimizing these parameters, an increase in the blood circulation time or a change in biodistribution can be achieved [47]. For example, the PEGylation of liposomes is a good example of when the blood circulation time was increased [48,49]. Another good example is the influence of the MNP size on their blood circulation time and biodistribution [50]. However, these approaches require the chemical structure of the nanoparticles to be optimized during synthetic procedures, and, once obtained, the nanoparticles' interaction with the cells cannot be regulated.

It is possible, however, to regulate the MNPs' unique interaction with cells by applying external magnetic fields. One of the best examples is magnetofection, an approach that allows a significant increase DNA and RNA delivery, through an increased MNP internalization by the cells. However, an increase in cell uptake is not always required, especially when the uptake by macrophages after intravenous injection of MNPs is considered.

The increase in the MNPs' uptake in the cells is influenced by their accumulation near the cell membrane, which increases the transmembrane transport effectiveness through different endocytosis mechanisms or simple diffusion through the membrane after applying a magnetic-field gradient [51]. In all in vitro experiments, magnets are oriented around the culture plate to create magnetic-field gradients that are perpendicular to the cell culture plane, leading to an accumulation of MNPs near the cell's surface. Conversely, during magnetomechanical actuation, the direction of the magnetic field changes according to the mechanical movement of magnets around the cells or by applying arrays of Helmholz coils. In these conditions, the MNPs may rotate and follow the changing direction of the external magnetic field before dissociating from the cell surface, resulting in a decrease in the cellular uptake. Apart from applying magnetic-field gradients, we also proved that the MNPs' magnetomechnical movement also plays a key role through our experiments, which were performed with a change in the magnet position from the top of the cell culture plate to the bottom. One can assume that when the magnet is located at the top of the cells, the MNPs are simply attracted by the magnetic-field gradient, thus reducing the local concentration around the cells and leading to the observed effects. However, the control experiments performed with a magnet located under the cells showed the same results, suggesting that MNP migration to or from the surface of the cells does not play a key role, but rather their mechanical movement in an LF DMF.

For each application, the magnetic core types for the best coatings can differ. It can be a small PEG-coating, which may contain free functional groups, or a thicker and more complicated coating for non-covalent interactions between the molecules and the nanoparticles, e.g., in drug delivery systems. The rate of the nanoparticles' interaction with the cells, and subsequent penetration into the cells, is an important detail. In our work, we chose Fe_3O_4 MNPs with two types of coating: DOPAC-PEG and DOPAC-HSA-PEG, which can be successfully used in magnetomechanical applications [52] and drug delivery systems, respectively [53]. The MNPs were incubated for different periods from 15 to 120 min in dynamic low-frequency magnetic fields. The average fluorescent intensity of the cells and the iron uptake measured with an MP-AES were both shown to decrease their cellular uptake after applying an external LF DMF. These results indicate the potential for a decreasing MNP uptake by the cells. Interestingly, 2 h of an LF DMF application reduced the MNP uptake by up to 46% in both cell lines. However, the total amount of MNPs internalized by the RAW264.7 cell line after the application of an LF DMF reduced from 0.82 to 0.49 pg Fe/cell, whereas for SH-SY5Y, it reduced from 0.19 to 0.09 pg Fe/cell.

5. Conclusions

Our results indicate that the application of an LF DMF can decrease MNPs' internalization in cell culture experiments. For both neuroblastoma and macrophage cell cultures, LF DMF application during cell incubation with MNPs decreases the MNP uptake. We believe that our observed results provide a new perspective on regulating the MNPs uptake by cells.

Supplementary Materials: The following supporting information can be downloaded at: https://www.mdpi.com/article/10.3390/magnetochemistry10020009/s1, Figure S1: (a) Histogram of MNPs core size distribution. (b) XRD pattern of Fe_3O_4@OA MNPs powder with Miller indices of the Bragg peaks in an inverse spinel structure (cps, counts per second). (c) Hydrodynamic diameter of Fe_3O_4-DOPAC-PEG-Cy5 and Fe_3O_4-DOPAC-HSA-PEG-Cy5 in PBS at pH = 7.4. (d) Hysteresis loop of MNP at T = 300 K. The specific magnetization was calculated using the Fe_3O_4 mass and the Fe content determined by the thermogravimetric analysis and AES analysis; Figure S2: Average intensity values of confocal images of SH-SY5Y cells areas in various incubation time with Fe_3O_4-DOPAC-HSA-PEG-Cy5 when magnetic field was applied from the top of the cells or under the cells, [Fe] = 100 ug/mL. *—*t*-test, significantly different ($p < 0.05$); Figure S3: Cytotoxicity assays of RAW264.7 and SH-SY5Y cells, which were incubated with Fe_3O_4-DOPAC-PEG-Cy5 and Fe_3O_4-DOPAC-HSA-PEG-Cy5 MNPs for 48 h; Figure S4: Prussian Blue staining of RAW264.7 cells; Figure S5: Prussian Blue staining of SH-SY5Y cells; Table S1: The hydrodynamic parameters of MNPs.

Author Contributions: Conceptualization, A.G.M. and M.A.A.; Formal analysis, A.V.I., N.S.C. and A.A.N.; Funding acquisition, V.P.C. and M.A.A.; Methodology, A.V.I., N.S.C. and A.A.N.; Software, A.A.N.; Supervision, A.G.M. and V.P.C.; Writing—original draft, A.V.I., N.S.C., A.A.N. and M.A.A. All authors have read and agreed to the published version of the manuscript.

Institutional Review Board Statement: Not applicable.

Informed Consent Statement: Not applicable.

Data Availability Statement: The data presented in this study are available upon request from the corresponding author.

Conflicts of Interest: The authors declare no conflicts of interest.

References

1. Jeon, M.; Halbert, M.V.; Stephen, Z.R.; Zhang, M. Iron Oxide Nanoparticles as T1 Contrast Agents for Magnetic Resonance Imaging: Fundamentals, Challenges, Applications, and Prospectives. *Adv. Mater.* **2021**, *33*, 1906539. [CrossRef] [PubMed]
2. Naumenko, V.; Garanina, A.; Nikitin, A.; Vodopyanov, S.; Vorobyeva, N.; Tsareva, Y.; Kunin, M.; Ilyasov, A.; Semkina, A.; Chekhonin, V.; et al. Biodistribution and Tumors MRI Contrast Enhancement of Magnetic Nanocubes, Nanoclusters, and Nanorods in Multiple Mice Models. *Contrast Media Mol. Imaging* **2018**, *2018*, 8264208. [CrossRef] [PubMed]
3. Caspani, S.; Magalhães, R.; Araújo, J.P.; Sousa, C.T. Magnetic Nanomaterials as Contrast Agents for MRI. *Materials* **2020**, *13*, 2586. [CrossRef]
4. Nori, Z.Z.; Bahadori, M.; Moghadam, M.; Tangestaninejad, S.; Mirkhani, V.; Mohammadpoor-Baltork, I.; Jafari, S.S.; Emamzadeh, R.; Alem, H. Synthesis and characterization of a new gold-coated magnetic nanoparticle decorated with a thiol-containing dendrimer for targeted drug delivery, hyperthermia treatment and enhancement of MRI contrast agent. *J. Drug Deliv. Sci. Technol.* **2023**, *81*, 104216. [CrossRef]
5. Neto, D.M.A.; da Costa, L.S.; de Menezes, F.L.; Fechine, L.M.U.D.; Freire, R.M.; Denardin, J.C.; Bañobre-López, M.; Vasconcelos, I.F.; Ribeiro, T.S.; Leal, L.K.A.M.; et al. A novel amino phosphonate-coated magnetic nanoparticle as MRI contrast agent. *Appl. Surf. Sci.* **2021**, *543*, 148824. [CrossRef]
6. Periyathambi, P.; Sastry, T.P.; Anandasadagopan, S.K.; Manickavasagam, K. Macrophages mediated diagnosis of rheumatoid arthritis using fibrin based magnetic nanoparticles as MRI contrast agents. *Biochim. Biophys. Acta—Gen. Subj.* **2017**, *1861*, 2992–3001. [CrossRef]

7. Chang, D.; Lim, M.; Goos, J.A.C.M.; Qiao, R.; Ng, Y.Y.; Mansfeld, F.M.; Jackson, M.; Davis, T.P.; Kavallaris, M. Biologically targeted magnetic hyperthermia: Potential and limitations. *Front. Pharmacol.* **2018**, *9*, 831. [CrossRef] [PubMed]

8. Włodarczyk, A.; Gorgoń, S.; Radoń, A.; Bajdak-Rusinek, K. Magnetite Nanoparticles in Magnetic Hyperthermia and Cancer Therapies: Challenges and Perspectives. *Nanomaterials* **2022**, *12*, 1807. [CrossRef]

9. Garanina, A.S.; Naumenko, V.A.; Nikitin, A.A.; Myrovali, E.; Petukhova, A.Y.; Klimyuk, S.V.; Nalench, Y.A.; Ilyasov, A.R.; Vodopyanov, S.S.; Erofeev, A.S.; et al. Temperature-controlled magnetic nanoparticles hyperthermia inhibits primary tumor growth and metastases dissemination. *Nanomed. Nanotechnol. Biol. Med.* **2020**, *25*, 102171. [CrossRef]

10. Tewari, A.B.; Sharma, R.; Sharma, D. Magnetic hyperthermia cancer therapy using rare earth metal-based nanoparticles: An investigation of Lanthanum strontium Manganite's hyperthermic properties. *Results Eng.* **2023**, *20*, 101537. [CrossRef]

11. Wang, Z.; Zhu, S.; An, L.; Tian, Q. Surface-structure-dependent magnetic hyperthermia performance of small Fe nanoparticles. *Mater. Lett.* **2023**, *339*, 134071. [CrossRef]

12. Qiao, R.; Fu, C.; Forgham, H.; Javed, I.; Huang, X.; Zhu, J.; Whittaker, A.K.; Davis, T.P. Magnetic iron oxide nanoparticles for brain imaging and drug delivery. *Adv. Drug Deliv. Rev.* **2023**, *197*, 114822. [CrossRef] [PubMed]

13. Kiani, A.; Davar, F.; Bazarganipour, M. Influence of verjuice extract on the morphology, phase, and magnetic properties of green synthesized CoFe2O4 nanoparticle: Its application as an anticancer drug delivery. *Ceram. Int.* **2022**, *48*, 34895–34906. [CrossRef]

14. Aslam, H.; Shukrullah, S.; Naz, M.Y.; Fatima, H.; Hussain, H.; Ullah, S.; Assiri, M.A. Current and future perspectives of multifunctional magnetic nanoparticles based controlled drug delivery systems. *J. Drug Deliv. Sci. Technol.* **2022**, *67*, 102946. [CrossRef]

15. Ulbrich, K.; Holá, K.; Šubr, V.; Bakandritsos, A.; Tuček, J.; Zbořil, R. Targeted Drug Delivery with Polymers and Magnetic Nanoparticles: Covalent and Noncovalent Approaches, Release Control, and Clinical Studies. *Chem. Rev.* **2016**, *116*, 5338–5431. [CrossRef]

16. Williams, P.S.; Moore, L.R.; Joshi, P.; Goodin, M.; Zborowski, M.; Fleischman, A. Microfluidic chip for graduated magnetic separation of circulating tumor cells by their epithelial cell adhesion molecule expression and magnetic nanoparticle binding. *J. Chromatogr. A* **2021**, *1637*, 461823. [CrossRef]

17. Haghighi, A.H.; Khorasani, M.T.; Faghih, Z.; Farjadian, F. Effects of different quantities of antibody conjugated with magnetic nanoparticles on cell separation efficiency. *Heliyon* **2020**, *6*, e03677. [CrossRef]

18. Haghighi, A.H.; Faghih, Z.; Khorasani, M.T.; Farjadian, F. Antibody conjugated onto surface modified magnetic nanoparticles for separation of HER2+ breast cancer cells. *J. Magn. Magn. Mater.* **2019**, *490*, 165479. [CrossRef]

19. Plouffe, B.D.; Murthy, S.K.; Lewis, L.H. Fundamentals and application of magnetic particles in cell isolation and enrichment: A review. *Rep. Prog. Phys.* **2015**, *78*, 016601. [CrossRef] [PubMed]

20. Tang, C.; He, Z.; Liu, H.; Xu, Y.; Huang, H.; Yang, G.; Xiao, Z.; Li, S.; Liu, H.; Deng, Y.; et al. Application of magnetic nanoparticles in nucleic acid detection. *J. Nanobiotechnol.* **2020**, *18*, 62. [CrossRef]

21. Roca, A.G.; Gutiérrez, L.; Gavilán, H.; Fortes Brollo, M.E.; Veintemillas-Verdaguer, S.; del Puerto Morales, M. Design strategies for shape-controlled magnetic iron oxide nanoparticles. *Adv. Drug Deliv. Rev.* **2019**, *138*, 68–104. [CrossRef]

22. Arsianti, M.; Lim, M.; Marquis, C.P.; Amal, R. Assembly of Polyethylenimine-Based Magnetic Iron Oxide Vectors: Insights into Gene Delivery. *Langmuir* **2010**, *26*, 7314–7326. [CrossRef]

23. Plank, C.; Schillinger, U.; Scherer, F.; Bergemann, C.; Rémy, J.S.; Krötz, F.; Anton, M.; Lausier, J.; Rosenecker, J. The magnetofection method: Using magnetic force to enhance gene delivery. *Biol. Chem.* **2003**, *384*, 737–747. [CrossRef]

24. Krötz, F.; de Wit, C.; Sohn, H.Y.; Zahler, S.; Gloe, T.; Pohl, U.; Plank, C. Magnetofection—A highly efficient tool for antisense oligonucleotide delivery in vitro and in vivo. *Mol. Ther.* **2003**, *7*, 700–710. [CrossRef]

25. Prosen, L.; Markelc, B.; Dolinsek, T.; Music, B.; Cemazar, M.; Sersa, G. Mcam Silencing with RNA Interference Using Magnetofection Has Antitumor Effect in Murine Melanoma. *Mol. Ther. Nucleic Acids* **2014**, *3*, e205. [CrossRef]

26. Jiang, M.; Liu, Q.; Zhang, Y.; Wang, H.; Zhang, J.; Chen, M.; Yue, Z.; Wang, Z.; Wei, X.; Shi, S.; et al. Construction of magnetic drug delivery system and its potential application in tumor theranostics. *Biomed. Pharmacother.* **2022**, *154*, 113545. [CrossRef]

27. Ota, S.; Takemura, Y. Characterization of Néel and Brownian Relaxations Isolated from Complex Dynamics Influenced by Dipole Interactions in Magnetic Nanoparticles. *J. Phys. Chem. C* **2019**, *123*, 28859–28866. [CrossRef]

28. Nguyen, L.H.; Phong, P.T.; Nam, P.H.; Manh, D.H.; Thanh, N.T.K.; Tung, L.D.; Phuc, N.X. The Role of Anisotropy in Distinguishing Domination of Néel or Brownian Relaxation Contribution to Magnetic Inductive Heating: Orientations for Biomedical Applications. *Materials* **2021**, *14*, 1875. [CrossRef] [PubMed]

29. Sadat, M.E.; Bud'ko, S.L.; Ewing, R.C.; Xu, H.; Pauletti, G.M.; Mast, D.B.; Shi, D. Effect of Dipole Interactions on Blocking Temperature and Relaxation Dynamics of Superparamagnetic Iron-Oxide (Fe$_3$O$_4$) Nanoparticle Systems. *Materials* **2023**, *16*, 496. [CrossRef]

30. Helbig, S.; Abert, C.; Sánchez, P.A.; Kantorovich, S.S.; Suess, D. Self-Consistent Solution of Magnetic and Friction Energy Losses of a Magnetic Nanoparticle. *Phys. Rev. B* **2023**, *107*, 054416. [CrossRef]

31. Nikitin, A.A.; Ivanova, A.V.; Semkina, A.S.; Lazareva, P.A.; Abakumov, M.A. Magneto-Mechanical Approach in Biomedicine: Benefits, Challenges, and Future Perspectives. *Int. J. Mol. Sci.* **2022**, *23*, 11134. [CrossRef]

32. Deissler, R.J.; Wu, Y.; Martens, M.A. Dependence of Brownian and Néel relaxation times on magnetic field strength. *Med. Phys.* **2014**, *41*, 012301. [CrossRef]

33. Winkler, R.; Ciria, M.; Ahmad, M.; Plank, H.; Marcuello, C. A Review of the Current State of Magnetic Force Microscopy to Unravel the Magnetic Properties of Nanomaterials Applied in Biological Systems and Future Directions for Quantum Technologies. *Nanomaterials* **2023**, *13*, 2585. [CrossRef]

34. Sievers, S.; Braun, K.F.; Eberbeck, D.; Gustafsson, S.; Olsson, E.; Schumacher, H.W.; Siegner, U. Quantitative Measurement of the Magnetic Moment of Individual Magnetic Nanoparticles by Magnetic Force Microscopy. *Small* **2012**, *8*, 2675. [CrossRef]

35. Allard-Vannier, E.; Hervé-Aubert, K.; Kaaki, K.; Blondy, T.; Shebanova, A.; Shaitan, K.V.; Ignatova, A.A.; Saboungi, M.-L.; Feofanov, A.V.; Chourpa, I. Folic acid-capped PEGylated magnetic nanoparticles enter cancer cells mostly via clathrin-dependent endocytosis. *Biochim. Biophys. Acta—Gen. Subj.* **2017**, *1861*, 1578–1586. [CrossRef]

36. Lee, S.H.; Park, D.J.; Yun, W.S.; Park, J.-E.; Choi, J.S.; Key, J.; Seo, Y.J. Endocytic trafficking of polymeric clustered superparamagnetic iron oxide nanoparticles in mesenchymal stem cells. *J. Control. Release* **2020**, *326*, 408–418. [CrossRef]

37. Behzadi, S.; Serpooshan, V.; Tao, W.; Hamaly, M.A.; Alkawareek, M.Y.; Dreaden, E.C.; Brown, D.; Alkilany, A.M.; Farokhzad, O.C.; Mahmoudi, M. Cellular uptake of nanoparticles: Journey inside the cell. *Chem. Soc. Rev.* **2017**, *46*, 4218–4244. [CrossRef]

38. Stratton, D.; Malibha-Pinchbeck, M.; Inal, J. Extremely low-frequency magnetic fields significantly enhance the cytotoxicity of methotrexate and can reduce migration of cancer cell lines via transiently induced plasma membrane damage. *Biochem. Biophys. Res. Commun.* **2022**, *626*, 192–199. [CrossRef] [PubMed]

39. Ramazi, S.; Salimian, M.; Allahverdi, A.; Kianamiri, S.; Abdolmaleki, P. Synergistic cytotoxic effects of an extremely low-frequency electromagnetic field with doxorubicin on MCF-7 cell line. *Sci. Rep.* **2023**, *13*, 8844. [CrossRef] [PubMed]

40. Merlot, A.M.; Kalinowski, D.S.; Richardson, D.R. Unraveling the mysteries of serum albumin-more than just a serum protein. *Front. Physiol.* **2014**, *5*, 108587. [CrossRef] [PubMed]

41. Nikitin, A.; Fedorova, M.; Naumenko, V.; Shchetinin, I.; Abakumov, M.; Erofeev, A.; Gorelkin, P.; Meshkov, G.; Beloglazkina, E.; Ivanenkov, Y.; et al. Synthesis, characterization and MRI application of magnetite water-soluble cubic nanoparticles. *J. Magn. Magn. Mater.* **2017**, *441*, 6–13. [CrossRef]

42. Li, X.; Hu, Y.; Xiao, J.; Cheng, D.; Xiu, Y.; Shi, H. Morphological Effect of Non-targeted Biomolecule-Modified MNPs on Reticuloendothelial System. *Nanoscale Res. Lett.* **2015**, *10*, 367. [CrossRef]

43. Zhang, M.; Gao, S.; Yang, D.; Fang, Y.; Lin, X.; Jin, X.; Liu, Y.; Liu, X.; Su, K.; Shi, K. Influencing factors and strategies of enhancing nanoparticles into tumors in vivo. *Acta Pharm. Sin. B* **2021**, *11*, 2265–2285. [CrossRef] [PubMed]

44. Portilla, Y.; Mulens-Arias, V.; Paradela, A.; Ramos-Fernández, A.; Pérez-Yagüe, S.; Morales, M.P.; Barber, D.F. The surface coating of iron oxide nanoparticles drives their intracellular trafficking and degradation in endolysosomes differently depending on the cell type. *Biomaterials* **2022**, *281*, 121365. [CrossRef] [PubMed]

45. Girardet, T.; Bianchi, E.; Henrionnet, C.; Pinzano, A.; Bouguet-Bonnet, S.; Boulogne, C.; Leclerc, S.; Cleymand, F.; Fleutot, S. SPIONs magnetic nanoparticles for MRI applications: Microwave synthesis and physicochemical, magnetic and biological characterizations. *Mater. Today Commun.* **2023**, *36*, 106819. [CrossRef]

46. Lin, H.; Yin, L.; Chen, B.; Ji, Y. Design of functionalized magnetic silica multi-core composite nanoparticles for synergistic magnetic hyperthermia/radiotherapy in cancer cells. *Colloids Surf. B Biointerfaces* **2022**, *219*, 112814. [CrossRef]

47. Takakura, Y.; Takahashi, Y. Strategies for persistent retention of macromolecules and nanoparticles in the blood circulation. *J. Control. Release* **2022**, *350*, 486–493. [CrossRef] [PubMed]

48. Couvreur, P.; Vauthier, C. Nanotechnology: Intelligent Design to Treat Complex Disease. *Pharm. Res.* **2006**, *23*, 1417–1450. [CrossRef] [PubMed]

49. Waghule, T.; Laxmi Swetha, K.; Roy, A.; Narayan Saha, R.; Singhvi, G. Exploring temozolomide encapsulated PEGylated liposomes and lyotropic liquid crystals for effective treatment of glioblastoma: In-vitro, cell line, and pharmacokinetic studies. *Eur. J. Pharm. Biopharm.* **2023**, *186*, 18–29. [CrossRef] [PubMed]

50. Khandhar, A.P.; Ferguson, R.M.; Arami, H.; Krishnan, K.M. Monodisperse magnetite nanoparticle tracers for in vivo magnetic particle imaging. *Biomaterials* **2013**, *34*, 3837–3845. [CrossRef]

51. Soledad Pereyra, A.; Mykhaylyk, O. Magnetofection Enhances Adenoviral Vector-based Gene Delivery in Skeletal Muscle Cells. *J. Nanomed. Nanotechnol.* **2016**, *7*, 364. [CrossRef] [PubMed]

52. Nikitin, A.A.; Arkhipov, V.A.; Chmelyuk, N.S.; Ivanova, A.V.; Vodopyanov, S.S.; Garanina, A.S.; Soldatov, M.A.; Gritsai, M.A.; Cherepanov, V.M.; Barbotina, N.N.; et al. Multifunctional Anisotropic Rod-Shaped CoFe$_2$O$_4$ Nanoparticles for Magnetic Resonance Imaging and Magnetomechanical Therapy. *ACS Appl. Nano Mater.* **2023**, *6*, 14540–14551. [CrossRef]

53. Semkina, A.; Nikitin, A.; Ivanova, A.; Chmelyuk, N.; Sviridenkova, N.; Lazareva, P.; Abakumov, M. 3,4-Dihydroxiphenylacetic Acid-Based Universal Coating Technique for Magnetic Nanoparticles Stabilization for Biomedical Applications. *J. Funct. Biomater.* **2023**, *14*, 461. [CrossRef] [PubMed]